Electronic Supplementary Material (ESI) for Environmental Science: Nano.

Supplementary Information

Regulating oxygen vacancy in ultrathin δ-MnO_2 nanosheets with superior activity for gaseous ozone decomposition

Ranran Cao [a], Lianxin Li [a], Pengyi Zhang [a, b *], Lele Gao [a] and Shaopeng Rong [c]

a. State Key Joint Laboratory of Environment Simulation and Pollution Control, School of Environment, Tsinghua University, Beijing 100084, China.

b. Beijing Key Laboratory for Indoor Air Quality Evaluation and Control, Beijing 100084, China.

c. Jiangsu Key Laboratory of Chemical Pollution Control and Resources Reuse, School of Environmental and Biological Engineering, Nanjing University of Science and Technology, Nanjing 210094, China.

---

[*] Corresponding author

E-mail address: zpy@tsinghua.edu.cn

Tel: +86-010-62796840

Details for some characterizations

The N_2 adsorption-desorption isotherms at 77 K were obtained with a Quantachrome physical adsorption apparatus (Autosorb-iQ3, USA). The specific surface area (S_{BET}) was calculated by the BET method and the pore volume (V_{pore}) was determined by the BJH method using the adsorption branch of the isotherm. The samples were degassed in vacuum at 200 ^{o}C for 4 h before measurements.

H_2-TPR and O_2-TPD were performed on a Micromeritics chemical adsorption instrument (AutoChem II 2920, USA). For H_2-TPR, 50 mg catalyst was pretreated at 105 °C in the atmosphere of He for 30 min. After cooled down to 40 °C, it was purged by 5% H_2/Ar for another 30 min to stabilize the baseline. Subsequently, it was heated up in the atmosphere of 5% H_2/Ar at the rate of 10 °C/min from 40 °C to 700 °C. For O_2-TPD, after the same pretreatment and cooled down to 40 °C, 50 mg catalyst was purged by 5% O_2/He for 30 min. Subsequently, when the baseline became stable under the helium flow, it was heated up from 40 °C to 900 °C at the rate of 10 °C/min and the gas products were monitored by the online mass spectrometer (Hiden Analytical HPR-20 R&D, Britain). For H_2-TPR and O_2-TPD experiments, an isopropyl alcohol / liquid nitrogen slurry was served as the cold trap to condense the possible water vapor before the emitted gases flowed into the thermal conductivity detector (TCD).

Theoretical calculations

Density functional theory (DFT) calculations were performed using the Vienna Ab-initio Simulation Package (VASP) code.[1−4] The generalized gradient approximation (GGA) with the Perdew–Burke–Ernzerhof (PBE) functional was adopted as the

exchange-correlation functional.[5,6] Ion–electron interactions were represented by ultrasoft pseudopotentials within the framework of the projector-augmented wave (PAW) method.[5] For the total energy calculations, the plane wave cutoff energy was 400 eV. The Brillouin zone integration was approximated by a sum over special selected k-points using the 3×3×1 MonkhorstPack method.[7] We optimized a monoclinic structure of MnO_2 (C2/m) with lattice constants of a = 5.149 Å, b = 2.843 Å, and c = 7.176 Å.[8] Due to the inaccuracy of standard DFT in describing the partially filled d-states in Mn^{3+} ions, the GGA+U formalism was used to correct the on-site Coulomb and exchange interactions for localized d orbitals and the values of U-J = 5.10 eV and J = 1.00 eV were adopted.[9] Because ultrathin δ-MnO_2 sub-microsheets mainly exposed (001) planes in the present work, the (001) surface slab was considered in this study. During the calculations, the bottom layer was fixed, and the other layers and the adsorbed species were relaxed. Moreover, in order to eliminate the interactions between slabs, the vacuum region was set to 15 Å in the z direction to separate the slabs. The geometries were optimized until the energy was converged to 1×10^{-5} eV/atom and the forces to 0.02 eV/Å.

The surface energy of pristine [MnO_6] sheet (γ_1) was obtained through the following equation:

$$\gamma_1 = \frac{E_{Slab}^{N} - N \cdot E_b}{2 \cdot A}$$

The surface energy of NH_4^+-adsorbed [MnO_6] sheet (γ_2) was calculated from the relation:[10]

$$\gamma_2 = \frac{E_{Slab}^{N+NH_4^+} - N \cdot E_b - E_{NH_4^+}^{Form}}{A} - \gamma_1$$

where E_{Slab}^{N} and $E_{Slab}^{N+NH_4^+}$ were the total energy of the clean slab and the NH_4^+-adsorbed slab with N formula units, respectively. E_b was the total energy of per formula unit of the bulk. A was the area of one slab surface. $E_{NH_4^+}^{Form}$ was the energy of the NH_4^+.

The adsorption energy (E_{ads}) of the adsorbate, i.e. O_3 or H_2O was obtained through the following equation:

$$E_{ads} = E_{total} - E_{basic} - E_{adsorbate},$$

where E_{total}, E_{basic} and $E_{adsorbate}$ were the total energy of the adsorption model, the energy of the clean slab and the energy of an isolated molecule of O_3 or H_2O, respectively.

The relative energy of each elementary step in ozone decomposition reaction was calculated according to equations (1)-(5).

$$V_O + O_3 \rightarrow *O_3 \quad (1)$$

$$*O_3 \rightarrow *O^{2-} + O_2(g) \quad (2)$$

$$*O^{2-} + O_3 \rightarrow *O^{2-} + *O_3 \quad (3)$$

$$*O^{2-} + *O_3 \rightarrow *O_2^{2-} + O_2(g) \quad (4)$$

$$*O_2^{2-} \rightarrow V_O + O_2(g) \quad (5)$$

Table S1. Catalytic activity of MnO_x catalysts for ozone decomposition

Catalyst	O_3 conc (ppm)	T (℃)	RH (%)	WHSV ($L\cdot g_{cat}^{-1}\cdot h^{-1}$)	Time (h)	O_3 conv (%)	Reaction rate ($\mu g\cdot g_{cat}^{-1}\cdot min^{-1}$)	Ref.
1M KOH-4h (α-MnO_2)	50	25	22	540	15	99	874.56	7
NaMn3 (α-MnO_2)	45	25	30	660	6	92.5	898.85	8
vac-200-4h (α-MnO_2)	20	25	30	540	12	48	169.61	9
Ce-γ-MnO_2	40	30	65	840	6	96	1037.94	10
Ce-MnO_x-2	100	25	50	540	10	100	1766.78	11
MnO_2-H2	45	25	50	600	6	91.3	806.53	15
H-MnO_2	115	25	50	600	5	60	1354.53	24
W-MnO_2	120	25	65	660	4	50	1295.64	40
Mn_3O_4/CNTs	50	25	50	1200	12	70.4	1382.01	43
$CeMn_{10}O_x$	40	30	65	840	6	99.5	1075.78	44
50-1-N-MnO_2	115	25	50	600	6	80	1806.04	45
MnO_2-N	**100**	**25**	**50**	**600**	**26**	**100**	**1963.09**	**This work**

Figure Captions

Figure S1. (a, b) AFM images of single ultrathin δ-MnO_2 sub-mcirosheet and relevant height profiles in (c).

Figure S2. SEM images of U-MnO_2 aged in the $(NH_4)_2SO_4$ solution (a) and in the NaCl solution (b).

Figure S3. Raman spectra of U-MnO_2, MnO_2-N, MnO_2-W and MnO_2-K.

Figure S4. (a-f) Time-dependent SEM images of the U-MnO_2 precursor aged in the NH_4Cl solution for 3 h, 6 h, 12 h, 24 h, 48 h and 72 h.

Figure S5. Schematic illustration of the formation of MnO_2-N.

Figure S6. The surface energies and schematic diagrams of (a) clean [MnO_6] sheet and (b) NH_4^+-adsorbed [MnO_6] sheet.

Figure S7. N_2 adsorption/desorption isotherms of (a) U-MnO_2, (b) MnO_2-N, (c) MnO_2-W and (d) MnO_2-K and the corresponding pore size distribution curves are shown in the insets.

Figure S8. FTIR patterns of U-MnO_2, MnO_2-N, MnO_2-W and MnO_2-K.

Figure S9. TG/DTG–MS curves of MnO_2-N

Figure S10. Water adsorption isotherms of MnO_2-N and MnO_2-K.

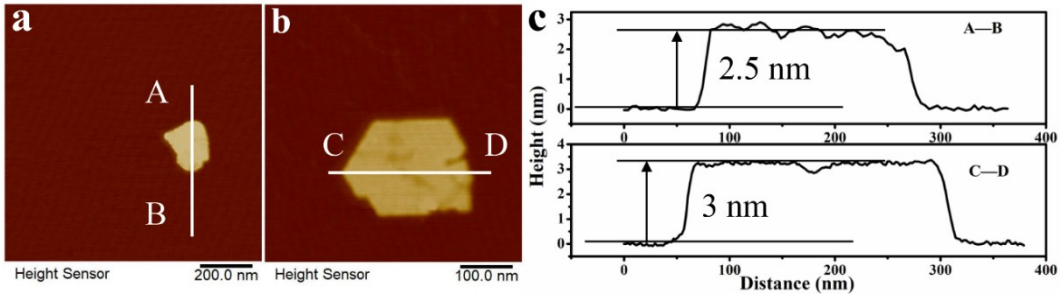

Figure S1 (a, b) AFM images of single ultrathin δ-MnO_2 sub-mcirosheet and relevant height profiles in (c).

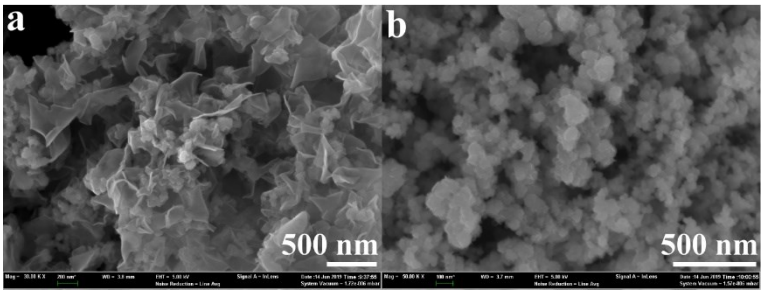

Figure S2. SEM images of U-MnO_2 aged in the $(NH_4)_2SO_4$ solution (a) and in the NaCl solution (b).

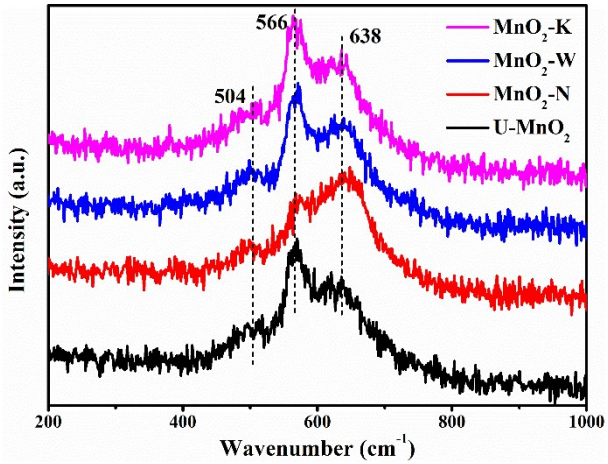

Figure S3. Raman spectra of U-MnO_2, MnO_2-N, MnO_2-W and MnO_2-K.

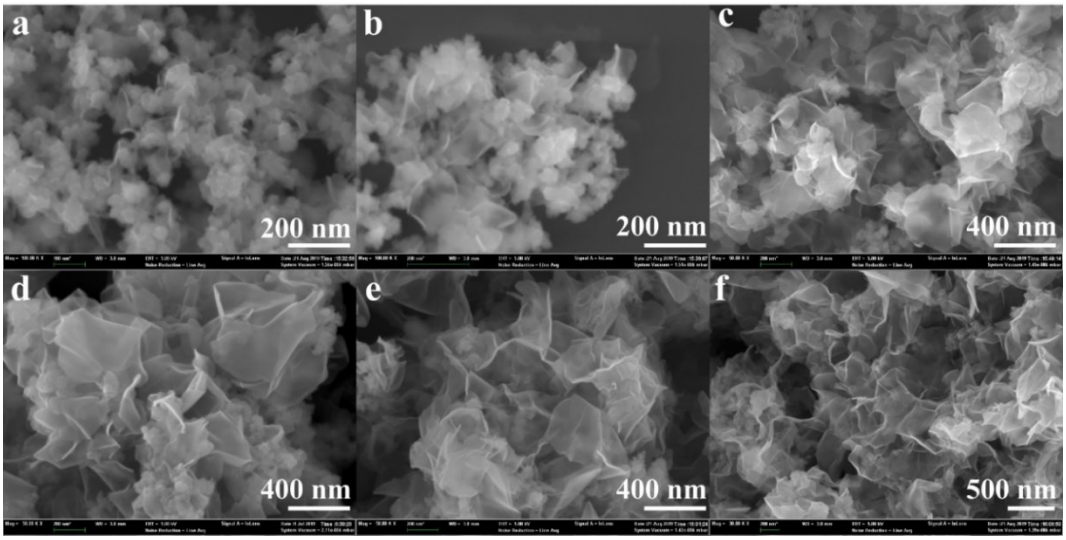

Figure S4. (a-f) Time-dependent SEM images of the U-MnO_2 precursor aged in the NH_4Cl solution for 3 h, 6 h, 12 h, 24 h, 48 h and 72 h.

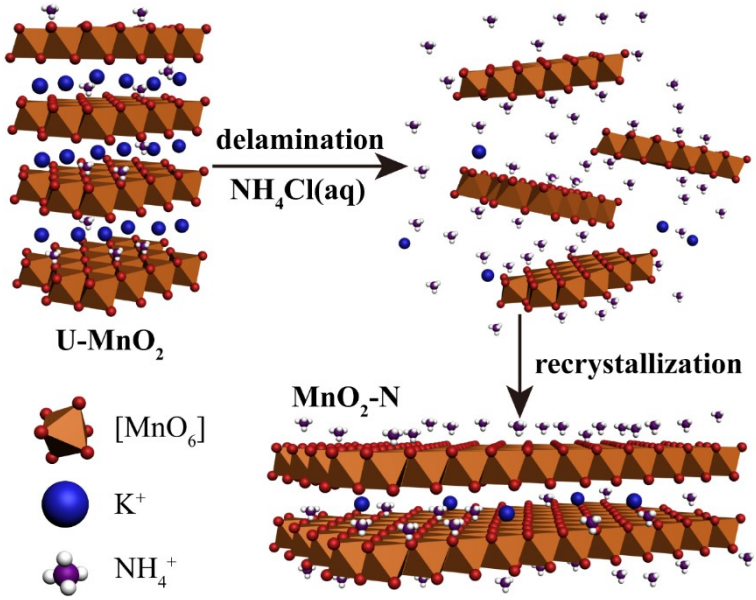

Figure S5. Schematic illustration of the formation of MnO_2-N.

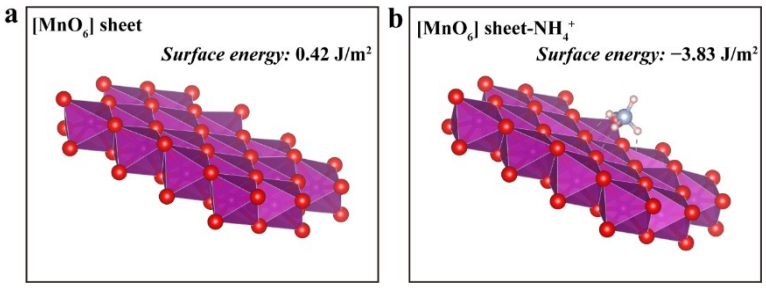

Figure S6. The surface energies and schematic diagrams of (a) clean [MnO_6] sheet and (b) NH_4^+-adsorbed [MnO_6] sheet.

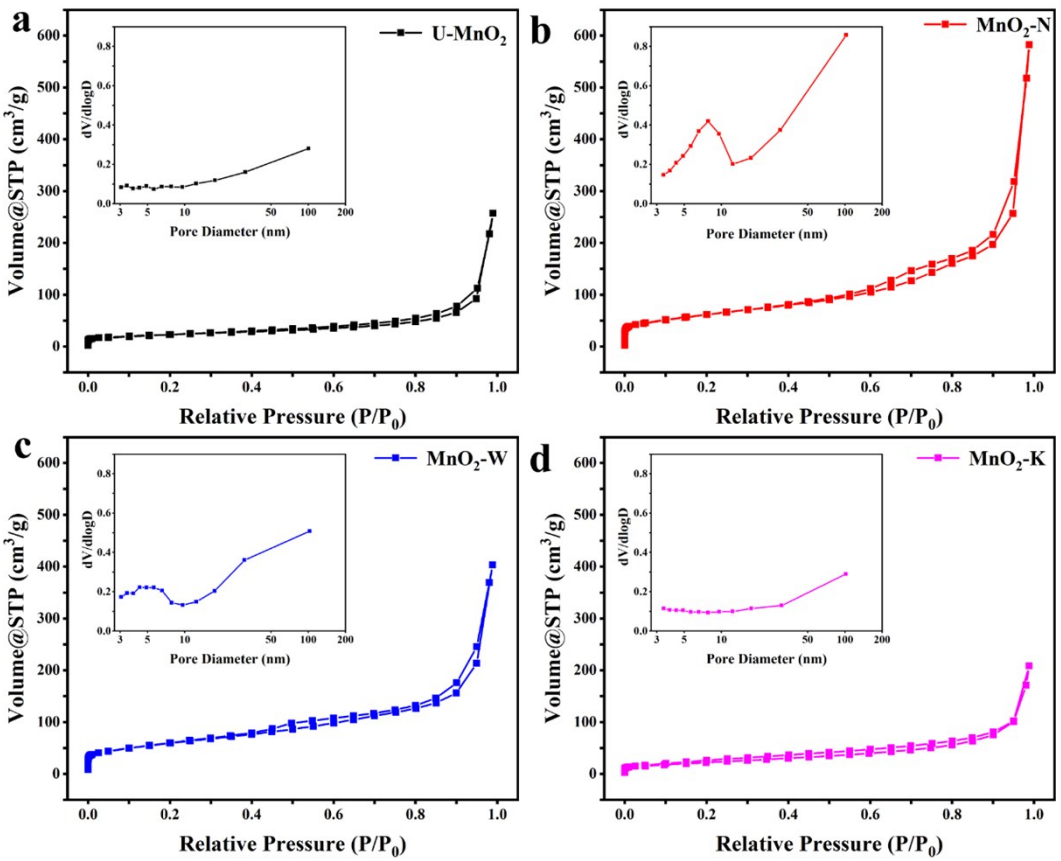

Figure S7. N_2 adsorption/desorption isotherms of (a) U-MnO_2, (b) MnO_2-N, (c) MnO_2-W and (d) MnO_2-K and the corresponding pore size distribution curves are shown in the insets.

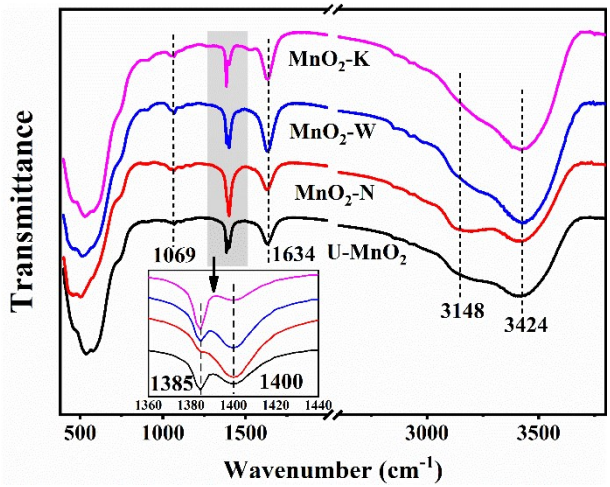

Figure S8. FTIR patterns of U-MnO_2, MnO_2-N, MnO_2-W and MnO_2-K.

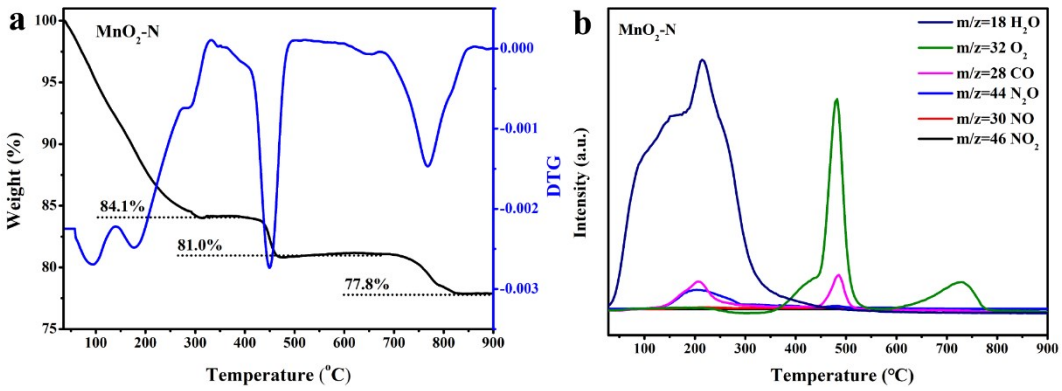

Figure S9. TG/DTG–MS curves of MnO_2-N

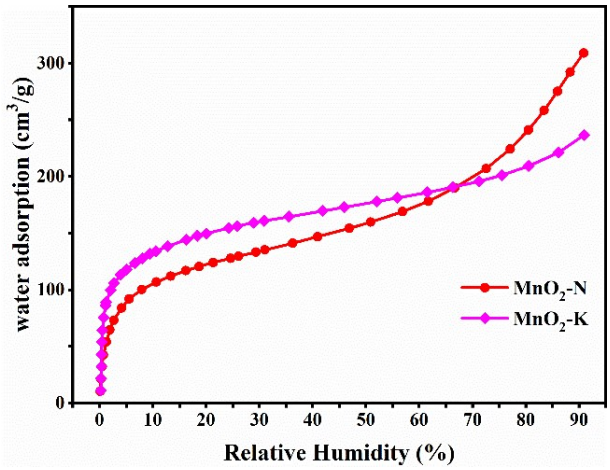

Figure S10. Water adsorption isotherms of MnO_2-N and MnO_2-K.

References

1 G. Kresse and J. Furthmüller, Efficiency of ab-initio total energy calculations for metals and semiconductors using a plane-wave basis set, Comp. Mater. Sci., 1996, 6, 15-50.

2 G. Kresse and J. Furthmüller, Efficient iterative schemes for ab-initio total energy calculations using a plane-wave basis set, Phys. Rev. B., 1996, 54, 11169-11186.

3 P. Hohenberg, Inhomogeneous electron gas, Phys. Rev., 1964, 136, B864-B871.

4 W. Kohn and L. J. Sham, Self-consistent equations including exchange and correlation effects, Phys. Rev., 1965, 140, A1133-A1138.

5 P. E. Blochl, Projector augmented-wave method, Phys. Rev. B., 1996, 50, 17953-17979.

6 J. P. Perdew, K. Burke and M. Ernzerhof, Generalized gradient approximation made simple, Phys. Rev. Lett., 1996, 77, 3865-3868.

7 H. J. Monkhorst and J. D. Pack, Special points for brillonin-zone integrations, Phys. Rev. B., 1976, 13, 5188-5192.

8 L. Miao, Q. Nie, J. Wang, G. Zhang and P. Zhang, Ultrathin MnO_2 nanosheets for optimized hydrogen evolution via formaldehyde reforming in water at room temperature, Appl. Catal. B: Environ., 2019, 248, 466-476.

9 D. A. Tompsett, S. C. Parker and M. S. Islam, Rutile (β-)MnO_2 surfaces and vacancy formation for high electrochemical and catalytic performance, J. Am. Chem. Soc., 2014, 136, 1418-1426.

10 R. E. Abutbul, E. Segev, U. Argaman, A. Tegze, G. Makov and Y. Golan, Stability of cubic tin sulphide nanocrystals: role of ammonium chloride surfactant headgroups, Nanoscale, 2019, 11, 17104-17110.